Research Square

Preprints are preliminary reports that have not undergone peer review.
They should not be considered conclusive, used to inform clinical practice,
or referenced by the media as validated information.

Deep Learning and Multi-Omics for Lung Cancer TME Risk Stratification

Xinyue Han
Heze Municipal Hospital
Hongjing Liu
Heze Municipal Hospital
Tan Liu
Heze Municipal Hospital
Xiang Lv
Shandong Tumor Hospital
Shuanghu Yuan
University of Science and Technology of China
Hongping Shi
Heze Municipal Hospital
Kang Wang
wangk101098@163.com

Heze Municipal Hospital

Research Article

Keywords: elderly lung cancer, immune microenvironment, deep learning, CT imaging, multi-omics, risk stratification, tumor microenvironment, public databases

Posted Date: November 13th, 2026

DOI: https://doi.org/10.21203/rs.3.rs-11177318/v1

License: This work is licensed under a Creative Commons Attribution 4.0 International License.
Read Full License

Additional Declarations: No competing interests reported.

Deep Learning and Multi-Omics for Lung Cancer TME Risk Stratification

Xinyue Han [a,b], Hongjing Liu [a], Tan Liu [a], Xiang Lv [c], Shuanghu Yuan [d], Hongping Shi [a,*], Kang Wang [a,*]

a Department of Medical Oncology, Heze Municipal Hospital, Heze, Shandong, China
b Department of Clinical Research, Shandong Cancer Hospital and Institute, Shandong First Medical University and Shandong Academy of Medical Sciences, Jinan, Shandong, China
c Department of Pathology, Shandong Cancer Hospital and Institute, Shandong First Medical University and Shandong Academy of Medical Sciences, Jinan, Shandong, China
d Department of Radiation Oncology, The First Affiliated Hospital of USTC, Division of Life Sciences and Medicine, University of Science and Technology of China, Hefei, Anhui, China

* Corresponding author:
Kang Wang
Department of Medical Oncology, Heze Municipal Hospital, Heze, Shandong, China, No 2888 Caozhou Road, Heze, Shandong, 274000, China.
Tel: 86-13021729819
Email: wangk101098@163.com

Hongping Shi
Department of Medical Oncology, Heze Municipal Hospital, Heze, Shandong, China, No 2888 Caozhou Road, Heze, Shandong, 274000, China.
Tel: 86-15853007287
Email: 115434263@qq.com

Abstract

Objective: Immune checkpoint inhibitors are increasingly used in elderly lung cancer patients, yet treatment response varies widely due to tumor immune microenvironment (TME) heterogeneity.

This study aimed to develop a CT image-based deep learning model for TME risk stratification in elderly patients (≥60 years) and to explore the underlying imaging-transcriptomic mechanisms.

Methods: Transcriptomic and clinical data for 436 elderly lung cancer patients were obtained from TCGA, with matched CT images from TCIA. Tumor segmentation was performed using nnU-Net, followed by feature extraction via a 3D residual network. The DeepSurv model was constructed combining imaging features with clinical variables. Multi-omics analyses included differential expression, functional enrichment, immune microenvironment assessment (CIBERSORT/ESTIMATE/ssGSEA), WGCNA, and Lasso-Cox regression. External validation used ICGC and GEO immunotherapy datasets.

Results: The nnU-Net model achieved a Dice coefficient of 0.858. The DeepSurv fusion model attained a C-index of 0.748, outperforming clinical models (0.668). High-risk patients had significantly shorter median overall survival than low-risk patients (13.4 vs. 23.8 months, $P < 0.001$). A 12-gene signature was identified, enriched in extracellular matrix remodeling, TGF-β signaling, and epithelial-mesenchymal transition. The high-risk group exhibited increased M2 macrophage and regulatory T-cell infiltration with reduced $CD8^+$ T cells, indicating an immunosuppressive phenotype. The signature stratified survival in the ICGC cohort ($P = 0.002$). Imaging-molecular correlation confirmed that imaging features reflect key immunosuppressive mechanisms.

Conclusion: This CT-based deep learning model effectively identifies elderly lung cancer patients with an immunosuppressive TME, offering superior risk stratification over traditional models. The imaging-molecular correlation supports CT imaging as a potential non-invasive tool for TME assessment and immunotherapy decision-making in elderly patients.

Keywords: elderly lung cancer; immune microenvironment; deep learning; CT imaging; multi-omics; risk stratification; tumor microenvironment; public databases

Introduction

Lung cancer is the malignant tumor with the highest incidence and mortality rates worldwide, with

non-small cell lung cancer (NSCLC) accounting for approximately 85% of all lung cancer cases [1]. With the accelerating global aging of the population, lung cancer has increasingly become a disease specific to the elderly; the median age at diagnosis is 71 years, and approximately 40% of patients are 75 years of age or older at the time of initial diagnosis [2]. Epidemiological data show that individuals aged 70 and older account for 43% of new NSCLC cases, and this proportion continues to rise as life expectancy increases [3]. Elderly lung cancer patients exhibit unique clinical characteristics, including a higher burden of comorbidities, organ dysfunction, polypharmacy, and frailty; these factors collectively complicate treatment decision-making and limit treatment options [4]. More critically, older patients have long been severely underrepresented in clinical trials; the proportion of older patients enrolled in the vast majority of pivotal registration trials is far lower than their actual proportion in the general population, leaving clinicians lacking high-level evidence-based medical guidance when developing treatment plans for this vulnerable population [5].

The advent of immune checkpoint inhibitors (ICIs) has profoundly transformed the treatment landscape for advanced NSCLC. By blocking immune evasion signaling pathways and restoring T cells' ability to recognize and eliminate tumor cells, PD-1/PD-L1 inhibitors have demonstrated significant survival benefits compared to conventional platinum-based dual-agent chemotherapy in multiple Phase III randomized controlled trials [6–8]. In the KEYNOTE-024 study, pembrolizumab monotherapy in patients with advanced NSCLC and high PD-L1 expression (tumor proportion score ≥50%) achieved a median overall survival of 30.0 months, more than double the 14.2 months observed in the chemotherapy group [6]. The KEYNOTE-042 study further expanded the population benefiting from this treatment to include patients with a PD-L1 score of ≥1% [7]. Regarding immunotherapy combined with chemotherapy, the KEYNOTE-189 study demonstrated that pembrolizumab combined with chemotherapy extended the median overall survival in patients with non-squamous NSCLC from 10.7 months to 22.0 months [8]. These landmark studies collectively established immunotherapy as the standard first-line treatment for advanced NSCLC. Of particular note, age subgroup analyses in the aforementioned studies consistently indicated that older patients (generally defined as ≥65 years) derived relative benefits from immunotherapy comparable to those of younger patients [6–8]. However, immunosenescence profoundly influences the response to immunotherapy in elderly NSCLC

patients—age-related declines in T-cell receptor repertoire diversity, increased proportions of regulatory T cells, and a chronic state of low-grade inflammation collectively constitute an immunosuppressive microenvironment specific to the elderly, which may lead to fundamental differences in the response patterns to ICIs between elderly and younger patients. Real-world studies further supplement the evidence from clinical trials.A large, multicenter retrospective study involving more than 4,000 elderly NSCLC patients showed that the median overall survival among elderly patients receiving immunotherapy reached 15.6 months, significantly outperforming the 9.8 months observed in those receiving single-agent chemotherapy [9]. A meta-analysis confirmed that immunotherapy significantly reduces the risk of death in patients aged 65 and older, with a hazard ratio of approximately 0.70 [10]. Regarding safety, studies indicate that there are no significant differences between elderly and younger patients in the incidence of immune-related adverse events of any grade or grade 3 and above [11,12]. However, rare but serious adverse events, such as immune-mediated myocarditis, occur at a slightly higher rate in elderly patients, and vigilance is warranted [13]. Nevertheless, significant treatment heterogeneity persists among elderly patients—approximately 40% to 60% of patients fail to achieve an objective response to immunotherapy, and some even experience disease hyperprogression [14]. The underlying cause of this treatment heterogeneity lies in individual differences in the tumor immune microenvironment (TME). Immunosenescence—that is, the age-related progressive decline in immune system function—profoundly influences the composition of the TME in elderly NSCLC patients. Aging is characterized by thymic atrophy, reduced initial T-cell output, accumulation of memory T cells, decreased T-cell receptor repertoire diversity, a chronic state of low-grade inflammation (inflammatory senescence), and functional changes in innate and adaptive immune cells [15]. In solid tumors, the immune status of the TME is typically classified into three categories: the immune-inflammatory type (infiltrating/“hot” tumors), the immune-exclusion type (where T cells cluster at the tumor periphery but fail to infiltrate), and the immune-desert type (“cold” tumors). Among these, immune-exclusion and immune-desert tumors exhibit significantly lower response rates to ICIs compared to the inflammatory type [16]. In elderly patients, abnormal activation of the TGF-β signaling pathway, excessive deposition of the extracellular matrix (ECM), and activation of cancer-associated fibroblasts (CAFs) collectively form physical and functional immune barriers that hinder the

effective infiltration of $CD8^+$ T cells [17]. Therefore, accurately assessing the TME status of elderly lung cancer patients—rather than making broad predictions about “treatment efficacy”—is a key prerequisite for achieving personalized immunotherapy. However, the predictive power of single biomarkers or simple scoring systems remains limited. More importantly, there is currently a lack of immunotherapy prognostic prediction tools specifically designed for elderly lung cancer patients that integrate multidimensional data (imaging, clinical, and molecular) [18].

Deep learning technologies have demonstrated immense application potential in the field of medical image analysis, capable of automatically learning hierarchical feature representations from raw image data, making them particularly well-suited for capturing subtle and complex diagnostic information in medical images [19]. In the field of lung CT image analysis, the nnU-Net framework has become the benchmark model for medical image segmentation due to its adaptive configuration capabilities [20]. Three-dimensional convolutional neural networks can directly process 3D CT volumetric data, fully leveraging information on tumor spatial heterogeneity [21]. In the field of lung cancer immunotherapy, previous studies have explored deep learning models based on CT images to predict the efficacy of immunotherapy [22–24]. However, existing studies generally have small sample sizes, lack independent external validation, and there is currently no deep learning-based CT image prognostic prediction model specifically designed for elderly lung cancer patients aged 60 and older[25]. Meanwhile, bioinformatics methods are playing an increasingly important role in the study of tumor immune mechanisms. Public databases such as TCGA, GEO, and ICGC provide valuable resources for large-scale biomarker discovery [26], and algorithms such as CIBERSORT and ESTIMATE have been widely used to infer tumor immune microenvironment characteristics from transcriptomic data [27,28]. WGCNA, which identifies gene modules that co-express in a highly coordinated manner by constructing gene co-expression networks, has been successfully applied to identify core driver genes in various tumor types [29]. However, existing bioinformatics studies have primarily focused on the general population across all age groups, and there is a significant lack of TME imaging assessment models specifically tailored for elderly lung cancer patients [30].

In summary, although immunotherapy has become an important treatment modality for elderly patients with advanced lung cancer, clinicians face the challenge of a lack of precise TME assessment tools specifically designed for the elderly population. Existing clinical biomarkers

cannot comprehensively reflect the complex state of the TME, while both CT-image-based deep learning models and bioinformatics analyses based on public databases have yet to systematically focus on the elderly patient population, and the mechanisms underlying the image-molecular correlation remain unclear. Combining deep learning techniques with bioinformatics methods to construct a TME risk stratification model specifically tailored for elderly lung cancer patients and to explore its image-transcriptomic correlation mechanisms holds promise for filling this significant research gap.

This study aims to construct a TME risk stratification model specifically for elderly lung cancer patients (≥60 years old) based on public databases and to elucidate its imaging-molecular association mechanisms: by utilizing TCGA transcriptomic and clinical data along with TCIA-CT imaging data, we will construct a deep learning-based imaging risk stratification model; the high-risk phenotype defined by this model corresponds, at the molecular level, to ECM remodeling, TGF-β signaling activation, and increased infiltration of immunosuppressive cells;simultaneously, using public databases such as TCGA, GEO, and ICGC, we systematically explored the molecular essence of the high-risk phenotype through bioinformatics methods including differential expression analysis, immune microenvironment assessment, weighted gene co-expression network analysis, and the construction of multigene risk profiles; we then validated the association between multigene risk profiles and clinical outcomes of immunotherapy using the GEO immunotherapy dataset; Furthermore, we integrated imaging phenotypes with molecular biomarkers based on paired samples to reveal the biological basis of imaging features as non-invasive assessment tools for the TME. Through this comprehensive research cycle—"imaging risk assessment—molecular mechanism analysis—validation of immunotherapy correlations—integration of imaging-molecular associations"—we provide a theoretical foundation and practical tools for personalized immunotherapy decision-making in elderly lung cancer patients.

Methods

1. Data Sources and Study Design

This study is a multi-omics retrospective analysis based on public databases. Using publicly

available transcriptomic data, clinical information, and CT imaging data, we constructed a risk stratification model for the TME in elderly lung cancer patients (≥60 years old) and explored its imaging-transcriptomic association mechanisms. The model aims to identify high-risk individuals with an immunosuppressive TME, thereby indirectly providing a basis for screening patients likely to benefit from immunotherapy.

Transcriptomic and clinical data were obtained from The Cancer Genome Atlas (TCGA) database (https://portal.gdc.cancer.gov/). RNA-sequencing data (in FPKM and counts formats) for lung adenocarcinoma (LUAD) and lung squamous cell carcinoma (LUSC), along with complete clinical follow-up information, were downloaded using the GDC client tool (version 1.6.1). Inclusion criteria were: (1) pathologically confirmed primary lung adenocarcinoma or lung squamous cell carcinoma; (2) age ≥ 60 years; (3) complete transcriptomic sequencing data; (4) complete survival follow-up information. Exclusion criteria were: (1) age < 60 years; (2) concomitant other malignancies; (3) incomplete clinical or follow-up information; (4) sequencing data of substandard quality. Since the TCGA database records the natural disease course without immunotherapy intervention, this study regarded overall survival (OS) in TCGA as a comprehensive reflection of intrinsic tumor aggressiveness and TME status, and used it as the risk label for model training. Data for validating immunotherapy-related associations were obtained from the Gene Expression Omnibus (GEO, https://www.ncbi.nlm.nih.gov/geo/). The screening criteria were: (1) expression profiling studies; (2) lung cancer tissue samples; (3) patients treated with immune checkpoint inhibitors; (4) sample size ≥ 30 cases; (5) provision of complete expression matrices and clinical information(including response assessment or progression-free survival). Ultimately, three datasets—GSE126044 (n=58), GSE135222 (n=42), and GSE156728 (n=36)—were included. A subgroup of patients aged ≥60 years (n=94) was extracted to validate the association between the model's risk stratification and clinical outcomes of immunotherapy.CT imaging data were obtained from The Cancer Imaging Archive (TCIA, https://www.cancerimagingarchive.net/). Pre-treatment chest CT images matching TCGA patients were retrieved from the TCGA-LUAD image set, the TCGA-LUSC image set, the NSCLC-Radiomics dataset (422 cases), and the LIDC-IDRI dataset (1,018 cases). The inclusion criteria for imaging data were: (1) matching the TCGA enrolled patient ID; (2) having complete pre-treatment chest CT images (DICOM format); (3) Image quality met the criteria; (4) Clear

tumor location annotations were present. External survival validation data were obtained from the International Cancer Genome Consortium (ICGC, https://dcc.icgc.org/), where whole-genome sequencing data for 118 lung cancer cases were retrieved. From these, 86 patients aged ≥60 years were selected to validate the ability of multigene features to stratify survival risk. Figure 1 shows the study design roadmap.

2. Data Preprocessing and Standardization

Transcriptomic data were standardized using the edgeR package (version 3.40.2), with the TMM method employed to calculate normalization factors and convert values to log2-CPM expression levels. For the GEO dataset, background correction and quantile normalization were performed using the RMA algorithm in the affy package (version 1.76.0), or the processed expression matrix was directly converted to log2 values.Batch effects were corrected using the ComBat algorithm (sva package, version 3.46.0), with the dataset source serving as the batch variable. The top 5,000 genes ranked by MAD were retained for subsequent WGCNA analysis. CT image preprocessing included: (1) resampling images to isotropic voxels (1 mm × 1 mm × 1 mm); (2) grayscale normalization to a uniform window width and level (window width: 1,500 HU; window level: −500 HU); (3) N4 bias field correction; (4) online data augmentation, including random rotation (±10°), random scaling (0.9–1.1x), random translation (±5 voxels), random elastic deformation, and horizontal flipping.

3. Automatic Tumor Segmentation

The nnU-Net framework (version 2) was used for automatic lung tumor segmentation. The TCIA image data were randomly split into training and validation sets in an 8:2 ratio.For the LIDC-IDRI dataset, existing annotations were used directly; for the NSCLC-Radiomics dataset, publicly available segmentation annotations were utilized; and for the TCGA-matched images, two radiologists with over 10 years of experience performed 3D manual segmentation using ITK-SNAP software, delineating tumor boundaries layer by layer. When there were inconsistencies between the mediastinal and lung windows, the lung window was taken as the standard, and discrepancies were resolved through consensus. A 3D U-Net architecture was adopted, with the encoder comprising five resolution levels, each containing two convolutional

layers (3×3×3 kernels) and one max-pooling layer (2×2×2 pooling window). The decoder restores spatial resolution through upsampling and concatenates the features with those from the corresponding encoder layers. The loss function is a weighted combination of Dice loss and cross-entropy loss (each weighted at 0.5). The Adam optimizer is used with an initial learning rate of 0.001, cosine-annealed decay, a maximum of 1,000 training iterations, and an early stopping strategy. Evaluation metrics include the Dice similarity coefficient, Hausdorff distance, and mean surface distance.

4. Deep Learning Feature Extraction and Prognostic Model Construction

A 3D Residual Network (3D ResNet) was used to extract deep learning features. The network consists of four residual modules with output channel counts of 64, 128, 256, and 512, respectively. A 512-dimensional feature vector was obtained through a global average pooling layer, and the network was pre-trained on the NSCLC-Radiomics dataset.Feature selection was performed using a three-step approach: (1) univariate Cox regression analysis to identify features with $P < 0.05$; (2) correlation analysis to exclude redundant features with a Pearson correlation coefficient > 0.85; (3) Lasso-Cox regression to determine the optimal λ value via 10-fold cross-validation and select features with non-zero coefficients. The DeepSurv model was constructed based on the selected imaging features combined with TCGA clinical variables (age, sex, histological type, and clinical stage). This model uses TCGA overall survival as the training label, and its output risk score is used to quantify the degree of immune suppression in the TME.The model employs the Cox proportional hazards loss function. The network architecture consists of three fully connected layers (with 256, 128, and 64 neurons, respectively), each followed by batch normalization, a ReLU activation layer, and a dropout layer (dropout rate of 0.3). The optimizer is Adam, with an initial learning rate of 0.001 and cosine-annealed decay; the model was trained for 150 epochs using an early stopping strategy.

5. Model Validation and Interpretability Analysis

Internal validation was performed using 10-fold cross-validation. Evaluation metrics included the C-index, time-dependent area under the receiver operating characteristic curve (time-dependent AUC, assessing 6-, 12-, and 24-month survival predictions), as well as the calibration curve and

Brier score. The SHAP method was used for interpretability analysis to calculate the mean absolute SHAP values for each feature to assess their importance, and SHAP dependency plots were used to visualize the relationship between key features and predicted risk.

6. Screening for Differentially Expressed Genes

Using the median overall survival of patients in the TCGA dataset as the cutoff, patients were divided into a low-risk group (survival time > median survival, operationally defined in this study as the group with lower TME immunosuppression) and a high-risk group (survival time ≤ median survival, operationally defined as the group with higher TME immunosuppression). The limma package (version 3.54.2) was used to perform differentially expressed gene (DEG) analysis, with group assignment as the categorical variable and adjustment for covariates such as age, sex, and histological type.The screening criteria were as follows: the absolute value of the $\log_2$ fold change ($\log_2$FC) > 1, and a false discovery rate (FDR) < 0.05 after correction using the Benjamin-Hochberg method. The results of the differential expression analysis were visualized using volcano plots (ggplot2 package, version 3.4.4) and clustering heatmaps (pheatmap package, version 1.0.12).

7. Functional Enrichment Analysis

To investigate the biological functions and related signaling pathways of differentially expressed genes, Gene Ontology (GO) functional enrichment analysis and Kyoto Encyclopedia of Genes and Genomes (KEGG) pathway enrichment analysis were performed separately for upregulated and downregulated genes. The analysis was performed using the clusterProfiler package (version 4.6.2), with the Human Genome Annotation Database (org.Hs.eg.db, version 3.16.0) serving as the background gene set. The GO analysis covered three categories: biological process (BP), cellular component (CC), and molecular function (MF). The significance threshold for the enrichment analysis was set at FDR < 0.05. The enrichment results were presented using bubble plots and bar charts.

8. Analysis of Tumor Immune Microenvironment Characteristics

To assess the infiltration of immune cells in the tumor microenvironment (TME), this study

employed multiple computational methods to enhance the reliability of the results.

(1) CIBERSORT Algorithm: Using the R implementation of CIBERSORT (https://cibersort.stanford.edu/), which is based on the principle of deconvolution, the gene expression matrix of tumor samples was matched with the LM22 reference gene expression feature matrix (containing characteristic genes for 22 immune cell subtypes) to infer the relative abundances of each immune cell subtype. The run parameters were set to 1,000 permutation tests, and only samples with $P < 0.05$ were retained for subsequent analysis. The Wilcoxon signed-rank test was used to compare differences in the proportions of various immune cell infiltrations between the high-risk group (group with higher TME immunosuppression) and the low-risk group (group with lower TME immunosuppression).

(2) ESTIMATE algorithm: The estimate package (version 1.0.13) was used to calculate the immune score, stromal score, and ESTIMATE score (the sum of the former two) for each sample. The immune score reflects the degree of immune cell infiltration, the stromal score reflects the degree of stromal cell infiltration, and the ESTIMATE score reflects the overall proportion of non-tumor components in the tumor tissue.Differences in scores between the two groups were compared using an independent samples t-test.

(3) Single-Sample Gene Set Enrichment Analysis (ssGSEA): Immune-related gene sets were downloaded from the Molecular Signatures Database (MSigDB, v7.5.1), including immune checkpoint gene sets, T-cell function-related gene sets, antigen presentation-related gene sets, interferon response-related gene sets, and TGF-β signaling pathway gene sets. The ssGSEA algorithm in the GSVA package (version 1.46.0) was used to calculate the enrichment scores for each gene set in every sample, and statistical significance was assessed using a permutation test (n = 1,000). Compare the differences in pathway enrichment scores between the two groups to identify immune pathways associated with prognosis. This analysis aims to directly verify whether the high-risk group exhibits an immunosuppressive or immune-exclusion phenotype at the cellular level (increased M2 macrophage infiltration, reduced $CD8^+$ T-cell infiltration, and elevated proportion of regulatory T cells), thereby confirming the biological validity of the TCGA overall survival grouping as a proxy for TME status.

9. Weighted Gene Co-expression Network Analysis

The WGCNA package (version 1.72-5) was used to construct gene co-expression networks. Using the top 5,000 genes ranked by MAD values as input, the optimal soft-thresholding power β was first selected using the pickSoftThreshold function, with the evaluation criterion set to a scale-free topological fit index (R^2) of 0.85 or higher.Based on the selected β value, the gene expression matrix was converted into a topological overlap matrix (TOM). Gene co-expression modules were then identified using the dynamic tree cut algorithm, with the following parameter settings: minimum module size (minModuleSize) = 50, and merge similarity threshold (mergeCutHeight) = 0.25. Module eigengenes (ME) were calculated for each module, and the correlations between these module eigengenes and clinical features (including overall survival, clinical stage, PD-L1 expression levels, etc.) were analyzed.For the module most strongly correlated with the target phenotype, the module membership (MM) and gene significance (GS) of each gene were calculated, and core genes were selected based on the criteria MM > 0.8 and |GS| > 0.3.

10. Construction and Validation of Multigene Risk Profiles

Based on all genes within the module identified by WGCNA as having the strongest association with overall survival, a multigene risk feature set was constructed using the Lasso-Cox regression method.Lasso regression was performed using the glmnet package (version 4.1-8), and the optimal regularization parameter λ was determined via 10-fold cross-validation (to minimize the partial likelihood error), selecting genes with non-zero regression coefficients. Based on this, a Cox proportional hazards regression model was constructed to calculate a risk score for each patient, calculated using the following formula:

Risk score = Σ(expression value of gene i × corresponding regression coefficient)

Using the median risk score from the TCGA training set as the cutoff value, patients were classified into high-risk and low-risk groups. Survival curves were plotted using the Kaplan-Meier method, and the log-rank test was used to compare differences in overall survival between the two groups.Time-dependent receiver operating characteristic (timeROC) curves were used to evaluate the discriminatory power of the prognostic feature in predicting 1-year, 2-year, and 3-year overall survival; the area under the curve (AUC) was calculated using the timeROC package (version 0.4).

The independent predictive value of this risk profile was validated using multivariate Cox

regression analysis, with adjustment for age, sex, histological type, and clinical stage. All survival analyses are presented as hazard ratios (HR) and their 95% confidence intervals (CI).

In the ICGC external validation cohort, risk scores were calculated for each patient using the same risk score formula, and patients were stratified by risk using the same median cutoff value. The aforementioned Kaplan-Meier survival analysis and time-dependent ROC analysis were repeated to validate the generalizability of this multigene risk profile. In the GEO immunotherapy dataset, risk scores were calculated for each patient using the same formula. Using the median cutoff value determined from the TCGA training set, patients were divided into high-risk and low-risk groups. Differences in progression-free survival (PFS) and objective response rate (ORR) following immunotherapy were compared between the two groups. Survival comparisons were performed using the Kaplan-Meier method and the log-rank test, while differences in ORR were compared using the χ^2 test. This analysis aims to verify whether the high-risk group defined by the model exhibits poorer clinical outcomes in a real-world immunotherapy cohort, thereby confirming the model's value in identifying individuals with an extremely low probability of benefiting from immunotherapy.

11. Construction of Protein-Protein Interaction Networks and Screening of Core Genes

The prognostic genes identified by the Lasso-Cox model were submitted to the STRING database (Search Tool for the Retrieval of Interacting Genes/Proteins, https://string-db.org/, version 11.5) to construct a protein-protein interaction (PPI) network. The interaction confidence threshold was set at 0.7 (high confidence). Cytoscape software (version 3.10.1) was used for network visualization and topological analysis. The following topological metrics were calculated for each node: (1) degree centrality, defined as the number of edges directly connected to the node; (2) betweenness centrality, defined as the proportion of all shortest paths in the network that pass through the node; (3) closeness centrality, defined as the reciprocal of the average length of the shortest paths from that node to all other nodes in the network. The top 5 genes ranked based on these three metrics were identified as core hub genes.

A single-gene survival analysis was performed on the core hub genes. Patients were divided into high-expression and low-expression groups using the median gene expression value as the cutoff, and the Kaplan-Meier method was used to compare differences in overall survival between the

two groups. Additionally, differences in the expression of core hub genes among patients at different clinical stages were compared using the Wilcoxon signed-rank test.

12. Association Analysis of Imaging Features and Molecular Biomarkers

To explore potential links between imaging phenotypes and molecular mechanisms, we conducted a cross-dataset association analysis between key molecular biomarkers identified through bioinformatics analysis and important imaging features previously identified using a deep learning model based on CT images.Specifically, the risk scores predicted by the deep learning model based on imaging data (derived from TCIA-CT imaging data) were correlated with gene expression data from 436 elderly lung cancer patients in the TCGA database. Spearman's rank correlation analysis was used to identify genes significantly associated with the imaging risk scores (FDR < 0.05), and the gene overlap rate between these genes and multigene prognostic features was calculated. We performed GO and KEGG functional enrichment analyses on the relevant genes and compared the consistency of their enriched pathways with those of differentially expressed genes. This analysis aims to verify whether radiological features reflect the molecular essence of ECM remodeling, TGF-β signaling activation, and an immunosuppressive TME, thereby providing molecular-level evidence for the use of CT imaging as a non-invasive tool for TME assessment.

13. Statistical Analysis

All statistical analyses in this study were performed using R software (version 4.3.2). Continuous variables are expressed as mean ± standard deviation (for normally distributed data) or median (interquartile range, P25–P75) (for non-normally distributed data); categorical variables are expressed as frequencies and percentages.Comparisons of continuous variables between groups were performed using the independent-samples t-test (for normally distributed data) or the Wilcoxon signed-rank test (for non-normally distributed data); comparisons of categorical variables were performed using the chi-square test or Fisher's exact test.Log-rank tests were used to compare survival curves. Cox proportional hazards regression models were used for univariate and multivariate analyses; the proportional hazards assumption was verified using the Schoenfeld residual test. If this assumption was violated, time-dependent coefficients or stratified Cox models

were used. All hypothesis tests were two-sided, with a significance level of $\alpha = 0.05$. The Benjamin-Hochberg method was used to control the FDR for multiple comparisons.

Results

1. Data Acquisition and Processing from Public Databases

Transcriptomic data and clinical information for patients with lung adenocarcinoma and lung squamous cell carcinoma were downloaded from the TCGA database. After rigorous screening, a total of 436 lung cancer patients aged ≥60 years were included, comprising 262 cases of lung adenocarcinoma (60.1%) and 174 cases of lung squamous cell carcinoma (39.9%). The median age of the patients was 68 years (interquartile range: 64–72 years); 284 were male (65.1%) and 152 were female (34.9%). The distribution by clinical stage was as follows: 102 cases (23.4%) were Stage I, 76 cases (17.4%) were Stage II, Stage III: 112 cases (25.7%), and Stage IV: 146 cases (33.5%). The median overall survival was 18.4 months (95% CI: 16.2–20.6 months), with 1-year, 2-year, and 3-year overall survival rates of 68.3%, 42.6%, and 28.1%, respectively.

Three lung cancer immunotherapy-related datasets were identified from the GEO database, including GSE126044 (n = 58), GSE135222 (n = 42), and GSE156728 (n = 36), comprising a total of 136 lung cancer patients who received immunotherapy. Among them, 94 patients (69.1%) aged ≥60 years were extracted, with a median OS of 14.6 months (95% confidence interval: 12.4–16.8 months). We obtained whole-genome sequencing data for 118 lung cancer patients from the ICGC database, of whom 86 were aged ≥60 years, with a median overall survival of 20.2 months. The clinical characteristics of each dataset are shown in Table 1.

2. Performance of the Automated Tumor Segmentation Model

The automatic lung tumor segmentation model built on the nnU-Net framework achieved good segmentation results on the validation set. After 862 training iterations, the model was stopped early, with a Dice coefficient of 0.896 on the training set and 0.872 on the validation set.When the automatic segmentation model was applied to the entire TCIA-CT image test set, compared with the manual segmentation gold standard, the average Dice coefficient for automatic segmentation was 0.858 ± 0.074, with a median of 0.872 and an interquartile range of 0.814–0.914. Other

evaluation metrics are as follows: the mean Hausdorff distance was 5.34 ± 3.12 mm, with a median of 4.80 mm; the mean surface distance was 1.44 ± 0.90 mm, with a median of 1.22 mm; the mean sensitivity was 0.874 ± 0.082, the mean specificity was 0.994 ± 0.004, and the mean accuracy was 0.983 ± 0.008. In a subgroup analysis based on tumor size (≤3 cm vs. >3 cm), the segmentation Dice coefficient for tumors >3 cm was significantly higher than that for tumors ≤3 cm (0.874 vs. 0.826, $P < 0.001$); in a subgroup analysis based on tumor location, the segmentation Dice coefficient for peripheral tumors was significantly higher than that for central tumors (0.872 vs. 0.838, $P < 0.001$) (Figure 2).

3. Deep Learning-Based Image Feature Extraction and Model Construction

A total of 512 deep learning features were extracted from each patient's CT images using a 3D residual network. Following feature extraction, univariate Cox regression analysis was performed, and 186 features met the selection criterion of $P < 0.05$. After excluding feature pairs with an absolute correlation coefficient > 0.85 via correlation analysis, 98 features remained.Lasso-Cox regression was then performed using 10-fold cross-validation to determine the optimal λ value of 0.039. At this λ value, 26 deep learning features with non-zero coefficients were selected for model construction. The coefficients of these 26 features ranged from -0.298 to 0.386; among them, 12 features had positive coefficients (associated with poor prognosis), and 14 features had negative coefficients (associated with favorable prognosis).

The DeepSurv model was constructed based on 26 deep learning image features and 4 clinical variables (age, sex, histological type, and clinical stage), with a total of 168,432 trainable parameters. The model underwent 150 training iterations, during which the training loss decreased from an initial value of 1.236 to a final value of 0.458, and the validation loss decreased from an initial value of 1.298 to a final value of 0.538. In a 10-fold cross-validation, the deep learning fusion model achieved an average C-index of 0.748 (95% CI: 0.704–0.792), which was significantly higher than the 0.668 (95% CI: 0.618–0.718,$P < 0.001$) and the Cox model based solely on imaging features (0.692; 95% CI: 0.644–0.740; $P = 0.003$). TimeROC analysis showed that the deep learning fusion model predicted mean AUCs of 0.806, 0.778, and 0.742 for 6-month, 12-month, and 24-month OS, respectively. Calibration curves indicated good agreement between predicted and observed 12-month survival probabilities, with a Brier score of 0.182.SHAP

analysis revealed that the top five features contributing most to the model's predictive power were, in order: clinical stage (mean absolute SHAP value 0.148), deep learning feature DLF_018 (0.142), age (0.118), deep learning feature DLF_045 (0.104), and histological type (0.082). A comparison of the performance of the various models is presented in Table 2.

Based on the risk scores predicted by the deep learning fusion model, patients were divided into a high-risk group (218 patients) and a low-risk group (218 patients) using the median risk score (0.456) among all 436 patients as the cutoff value. Kaplan-Meier survival analysis showed that the median OS for patients in the low-risk group was 23.8 months (95% CI: 20.4–27.2 months), while that for the high-risk group was 13.4 months (95% CI: 11.2–15.6 months); the difference was statistically significant ($P < 0.001$). The 1-year, 2-year, and 3-year OS rates in the low-risk group were 78.4%, 52.3%, and 34.9%, respectively, while those in the high-risk group were 58.3%, 32.6%, and 21.6%, respectively. Multivariate Cox regression analysis showed that the hazard ratio for the risk score was 2.76 (95% CI: 2.12–3.58, $P < 0.001$), and the HR for clinical stage was 1.84 (95% CI: 1.36–2.48, $P < 0.001$) (Figure 2).

4. Screening of Differentially Expressed Genes and Functional Enrichment Analysis

Using the median OS (18.4 months) of patients in the TCGA dataset as the cutoff, the 436 patients were divided into a low-risk group (survival time > 18.4 months, operationally defined in this study as the group with a lower degree of TME immunosuppression) and a high-risk group (survival time ≤ 18.4 months, operationally defined as the group with a higher degree of TME immunosuppression). Differentially expressed genes were analyzed using the limma package. After adjusting for age, sex, and histological type, a total of 487 differentially expressed genes were identified, of which 212 (43.5%) were upregulated and 275 (56.5%) were downregulated in the high-risk group. Among the upregulated genes, COL11A1 exhibited the highest fold change ($log2FC = 3.42$, $FDR < 0.001$), followed by THBS2 ($log2FC = 2.98$, $FDR < 0.001$) and MMP11 ($log2FC = 2.76$, $FDR < 0.001$); Among the downregulated genes, the one with the highest fold change was SFTPB ($log2FC = -1.64$, $FDR < 0.001$), followed by SFTPC ($log2FC = -1.40$, $FDR < 0.001$) and NAPSA ($log2FC = -1.29$, $FDR < 0.001$).

GO functional enrichment analysis showed that upregulated genes were significantly enriched in extracellular matrix ($FDR = 2.3 \times 10^{-12}$), collagen fiber organization ($FDR = 1.8 \times 10^{-9}$), cell

adhesion (FDR = 4.2×10^{-8}), angiogenesis (FDR = 3.6×10^{-7}), and epithelial-mesenchymal transition (FDR = 5.9×10^{-7});downregulated genes were significantly enriched in surfactant metabolism (FDR = 1.2×10^{-14}), alveolar development (FDR = 3.4×10^{-10}), gas exchange (FDR = 2.1×10^{-8}), and immune response regulation (FDR = 4.8×10^{-6}).KEGG pathway enrichment analysis revealed that upregulated genes were significantly enriched in extracellular matrix-receptor interactions (FDR = 2.6×10^{-8}), the PI3K-Akt signaling pathway (FDR = 4.8×10^{-7}), focal adhesion (FDR = 1.2×10^{-6}), the TGF-β signaling pathway (FDR = 3.4×10^{-5}), and the Wnt signaling pathway (FDR = 6.2×10^{-5}); Downregulated genes were significantly enriched in the complement and coagulation cascades (FDR = 1.8×10^{-6}), the PPAR signaling pathway (FDR = 3.2×10^{-5}), drug metabolism—cytochrome P450 (FDR = 2.6×10^{-4}), and retinol metabolism (FDR = 4.8×10^{-4}). These enrichment results suggest that the molecular characteristics of the high-risk group (i.e., the group with a higher degree of TME immunosuppression) are dominated by ECM remodeling, TGF-β signaling activation, and EMT; these pathways collectively constitute the molecular basis of the immunosuppressive TME (Figure 3).

5. Characteristics of the Tumor Immune Microenvironment

Analysis using the CIBERSORT algorithm revealed significant differences in immune infiltration between the low-risk group (the group with lower TME immunosuppression) and the high-risk group (the group with higher TME immunosuppression). In the low-risk group, the proportions of $CD8^+$ T cells (18.6% vs. 12.4%, $P < 0.001$), follicular helper T cells (8.2% vs. 5.6%, $P = 0.002$), M1 macrophages (6.8% vs. 4.2%, $P < 0.001$), and resting dendritic cells (4.6% vs. 3.2%, $P = 0.008$) were significantly higher in the low-risk group than in the high-risk group. In the high-risk group, the infiltration rates of M2 macrophages (14.2% vs. 8.6%, $P < 0.001$), regulatory T cells (6.8% vs. 4.4%, $P = 0.002$), resting mast cells (5.2% vs. 3.4%, $P = 0.004$), and neutrophils (4.8% vs. 3.0%, $P = 0.006$) were significantly higher in the high-risk group than in the low-risk group. Analysis using the ESTIMATE algorithm showed that the immune score (1246 ± 342 vs 986 ± 298, $P < 0.001$) and the ESTIMATE score (1684 ± 456 vs 1420 ± 388,$P < 0.001$) were significantly higher in the low-risk group than in the high-risk group; however, there was no statistically significant difference in the stroma score between the two groups (438 ± 168 vs. 434 ± 156, $P = 0.812$). ssGSEA analysis revealed that in the low-risk group, antigen presentation-related pathways

(enrichment score 0.32 vs. −0.18, P < 0.001), T-cell activation-related pathways (0.28 vs −0.12, P < 0.001), and the interferon-γ response pathway (0.24 vs −0.08, P = 0.002) were significantly higher in the low-risk group than in the high-risk group;in the high-risk group, the enrichment scores for the TGF-β signaling pathway (0.22 vs. −0.14, P = 0.004) and the hypoxia-related pathway (0.18 vs. −0.06, P = 0.018) were significantly higher than those in the low-risk group (Figure 4).

6. Weighted Gene Co-expression Network Analysis and Construction of Multigene Risk Profiles

A gene co-expression network was constructed using the WGCNA method, with a soft threshold power of β = 5 (scale-free topological fit index $R^2 = 0.86$). Twelve gene modules were identified using the dynamic pruning tree algorithm, ranging in size from 86 to 486 genes.Analysis of the correlation between each module and clinical features revealed that the blue module (386 genes) showed the strongest correlation with overall survival (r = −0.42, P = 2.6×10^{-6}) and was significantly correlated with PD-L1 expression levels (r = 0.38, P = 1.8×10^{-5}); the brown module (224 genes) was significantly associated with clinical stage (r = 0.36, P = 4.2×10^{-5}); and the blue-green module (168 genes) showed a weak correlation with age (r = 0.18, P = 0.032). Using the criteria of module membership > 0.8 and |gene significance| > 0.3, 34 core genes were selected from the blue module, including COL11A1, THBS2, MMP11, SPP1, POSTN, FN1, TIMP1, LOXL2, CTSK, and MMP14, which primarily encode extracellular matrix-related proteins and matrix metalloproteinases.

Based on the 386 genes in the blue module, Lasso-Cox regression with 10-fold cross-validation was used to identify 12 genes with non-zero coefficients to construct a multigene prognostic feature set: COL11A1, THBS2, MMP11, SPP1, POSTN, FN1, TIMP1, LOXL2, CTSK, MMP14, COMP, and IBSP.The regression coefficients and hazard ratios for each gene are shown in Table 3. A risk score was calculated for each patient based on the weighted expression of the 12 genes, and patients were classified into high-risk and low-risk groups using the median risk score from the TCGA training set as the cutoff value. Kaplan-Meier survival analysis showed that the median OS was 26.4 months (95% CI: 22.8–30.0) in the low-risk group and 12.8 months (95% CI: 10.6–15.0) in the high-risk group, with a statistically significant difference (log-rank P < 0.001). TimeROC

analysis showed that the AUCs for predicting 1-year, 2-year, and 3-year overall survival were 0.784, 0.762, and 0.738, respectively. In the ICGC external validation set (86 cases), this feature was also effective in distinguishing between high-risk and low-risk patients (log-rank P = 0.002), with an AUC of 0.756 for 1-year OS. Multivariate Cox regression analysis showed that this risk score was independent of age, sex, histological type, and clinical stage (HR = 2.42, 95% CI: 1.86–3.15, P < 0.001) (Figure 5 and Table 4).

7. Protein-Protein Interaction Network and Core Gene Screening

The 12 prognostic genes were submitted to the STRING database to construct a protein-protein interaction network, with a confidence threshold of ≥0.7. The network contained 12 nodes and 34 edges, with an average node degree of 5.67 and a network clustering coefficient of 0.742. Based on a ranking of degree centrality, betweenness centrality, and closeness centrality, the top five core hub genes were FN1 (degree centrality 9), COL11A1 (degree centrality 7), THBS2 (degree centrality 6), SPP1 (degree centrality 5), and MMP11 (degree centrality 5). Single-gene survival analysis showed that high expression of all five core genes was significantly associated with poor prognosis. The median overall survival was 14.2 months in the high-expression group for FN1 and 22.6 months in the low-expression group (P < 0.001);the median overall survival in the high-expression group for COL11A1 was 13.8 months, compared with 23.4 months in the low-expression group (P < 0.001); in the high-expression group for THBS2, it was 15.2 months, compared with 21.8 months in the low-expression group (P = 0.002); in the high-expression group for SPP1, it was 14.6 months, compared with 22.0 months in the low-expression group (P = 0.004); the MMP11 high-expression group was 15.0 months, and the low-expression group was 21.4 months (P = 0.006). The expression levels of these five genes were significantly higher in Stage IV patients than in Stage III patients (all P < 0.01) (Figure 6).

8. Association Analysis of Imaging Features and Molecular Biomarkers

A Spearman correlation analysis was performed between the imaging risk scores predicted by the deep learning model and TCGA gene expression data, identifying a total of 86 genes significantly

associated with high imaging risk scores (|r| > 0.3,FDR < 0.05). Among these, 8 genes overlapped with the multigene prognostic profile: COL11A1 (r = 0.42), THBS2 (r = 0.38), MMP11 (r = 0.36), SPP1 (r = 0.34), POSTN (r = 0.32), FN1 (r = 0.31), TIMP1 (r = 0.30), and LOXL2 (r = 0.28). The regression coefficients for these genes in the polygenic signature were all positive (0.128–0.284), with 100% directional consistency. Functional enrichment analysis was performed on the 86 imaging risk-associated genes,the results showed that these genes were significantly enriched in extracellular matrix remodeling (FDR = 2.4×10^{-8}), collagen metabolism (FDR = 1.6×10^{-6}), the TGF-β signaling pathway (FDR = 3.8×10^{-5}), and epithelial-mesenchymal transition (FDR = 2.2×10^{-4}), which closely aligns with the enriched pathways of differentially expressed genes. Based on these findings, the following hypothesis is proposed: The high-risk features identified by the deep learning model for CT imaging may reflect the level of extracellular matrix remodeling in the tumor. These biological processes are closely associated with increased M2 macrophage infiltration, reduced $CD8^+$ T-cell infiltration, and activation of the TGF-β signaling pathway, which collectively constitute an immunosuppressive tumor microenvironment, thereby leading to poor prognosis in elderly lung cancer patients (Figure 6).

Discussion

This study utilized public databases to construct a risk stratification model for the tumor immune microenvironment in elderly lung cancer patients and explored its molecular mechanisms, forming a closed-loop research cycle from imaging phenotypes to molecular explanations. The nnU-Net automatic segmentation model achieved good results (Dice = 0.858); the DeepSurv fusion model reached a C-index of 0.748, significantly outperforming traditional clinical models (0.668); the median survival in the high-risk group was 13.4 months, compared to 23.8 months in the low-risk group (P < 0.001). Bioinformatics analysis identified 487 differentially expressed genes and constructed a risk signature comprising 12 genes, primarily enriched in extracellular matrix remodeling, the TGF-β signaling pathway, and epithelial-mesenchymal transition; The high-risk group exhibited increased infiltration of M2 macrophages and regulatory T cells, along with reduced infiltration of CD8-positive T cells. Imaging-molecular correlation analysis identified 8 overlapping genes with highly consistent functional enrichment, suggesting that imaging-based

risk profiles may reflect the tumor's immunosuppressive microenvironment. This study represents the first effort to specifically develop a multi-omics-based TME risk stratification model for elderly lung cancer patients; the first systematic integration of CT imaging, transcriptomic, and clinical data from public databases to form a multi-omics predictive framework; and the first to reveal the biological essence underlying deep learning features from an imaging-molecular correlation perspective, providing a theoretical basis for model interpretability.

Immunotherapy has become an important treatment option for elderly patients with advanced lung cancer; however, due to significant clinical heterogeneity and immunosenescence in this population, accurately identifying patient subgroups suitable for immunotherapy while avoiding ineffective and overtreatment remains a pressing challenge in clinical practice [4,30]. The deep learning-based risk prediction model developed in this study holds significant clinical value in multiple aspects.

The predictive performance of this model surpasses that of traditional clinical models. In this study, the C-index of PD-L1 expression level as a single predictive indicator was only 0.684, whereas the C-index of the deep learning fusion model reached 0.748 in cross-validation, representing a significant improvement in predictive performance. This means that the model can more accurately identify elderly patients with an immunosuppressive TME who have an extremely low probability of benefiting from immunotherapy, as well as those whose prognosis remains poor even if they receive immunotherapy. This precise risk stratification helps optimize the allocation of medical resources and avoid the use of expensive immunotherapy drugs in patients for whom treatment is expected to be ineffective [18]. Based on routine pre-treatment chest CT images, the model offers the advantages of being non-invasive, reproducible, and easily accessible.Unlike PD-L1 testing or genetic sequencing, which require tumor tissue samples, CT imaging is a routine examination in the diagnosis and treatment of lung cancer patients and does not require additional invasive procedures. This gives the model excellent accessibility and potential for widespread adoption in clinical practice. By combining imaging features with clinical variables, the model can make predictions before immunotherapy is initiated, providing proactive guidance for treatment decisions. Compared to traditional biomarkers, deep learning models can automatically integrate information on tumor spatial heterogeneity—an important prognostic dimension that single-molecule biomarkers cannot capture. SHAP explainability analysis further revealed that

clinical stage, deep learning-derived imaging features, age, and histological type were the factors contributing most significantly to the model's predictions. The overall contribution of imaging features exceeded that of any single clinical variable, highlighting the unique value of imaging information in risk prediction.

The nnU-Net automatic segmentation model used in this study achieved a Dice coefficient of 0.858 on a public CT image dataset, which is comparable to the performance of automatic CT image segmentation for lung cancer reported in the literature [20]. Notably, the segmentation accuracy for peripheral tumors was significantly higher than that for central tumors (Dice: 0.872 vs. 0.838), which may be related to the blurred boundaries of central tumors with mediastinal structures and areas of atelectasis. The segmentation accuracy for tumors >3 cm was also superior to that for tumors ≤3 cm (0.874 vs. 0.826), suggesting that the precise segmentation of small tumors remains a technical challenge, which is consistent with the conclusions of previous studies.The application of automatic segmentation technology enables the batch processing of large-scale imaging data—manually tracing a single lung cancer CT scan layer by layer typically takes 15 to 30 minutes, whereas nnU-Net can complete 3D segmentation in a matter of seconds, with segmentation accuracy approaching that of manual methods. This technological advancement lays the technical foundation for constructing a deep learning-based prognostic prediction model in this study.

Regarding feature extraction, the 3D residual network employed in this study extracted 512 deep learning features from 3D CT volumes through four residual modules; these features encompassed multidimensional information such as tumor morphology, texture, and spatial heterogeneity. Through a three-step feature selection strategy (univariate Cox analysis, correlation filtering, and Lasso-Cox), 26 imaging features significantly associated with prognosis were ultimately identified. These features include both those reflecting the tumor's overall invasive phenotype (such as irregular borders and large volume) and textural features reflecting intratumoral heterogeneity. Previous studies have confirmed that intratumoral heterogeneity is closely associated with resistance to immunotherapy, and imaging features can non-invasively capture this heterogeneity [23]. The SHAP analysis in this study showed that multiple deep learning-derived imaging features contributed more to model predictions than traditional clinical variables, further validating the unique value of imaging features in prognostic assessment.

Through bioinformatics analysis of public databases, this study systematically explored the molecular mechanisms underlying the immunosuppressive state of the TME in elderly lung cancer patients.This study identified 487 differentially expressed genes significantly associated with the prognosis of lung cancer in the elderly. Functional enrichment analysis revealed that these genes are primarily involved in the extracellular matrix, epithelial-mesenchymal transition, the TGF-β signaling pathway, and the Wnt signaling pathway. These pathways play key roles in tumor progression and immune evasion. Extracellular matrix remodeling is a critical process in tumor invasion and metastasis, and it also influences the infiltration and function of immune cells [30]. Genes significantly upregulated in the high-risk group of this study included COL11A1, THBS2, MMP11, SPP1, POSTN, and FN1, all of which belong to the extracellular matrix-related gene family. COL11A1 encodes the α1 chain of collagen type XI, which is highly expressed in various malignant tumors and associated with poor prognosis; it promotes tumor invasion and metastasis by activating the TGF-β signaling pathway.THBS2 encodes thrombin-sensitive protein 2, an extracellular matrix glycoprotein that participates in the regulation of angiogenesis and immune modulation within the tumor microenvironment. MMP11 encodes matrix metalloproteinase 11, a member of the matrix metalloproteinase family that promotes tumor cell migration and invasion by degrading extracellular matrix components [31]. SPP1 encodes osteopontin, a multifunctional phosphorylated glycoprotein that recruits immunosuppressive cells and promotes M2 macrophage polarization in the tumor microenvironment [32]. The synergistic overexpression of these genes suggests active extracellular matrix remodeling in the high-risk group, which may constitute a physical barrier hindering immune cell infiltration while simultaneously creating an immunosuppressive microenvironment through the release of active factors.

KEGG pathway enrichment analysis revealed that the TGF-β signaling pathway was significantly activated in the high-risk group. TGF-β is a key immunosuppressive factor in the tumor microenvironment that induces regulatory T cell differentiation, suppresses CD8-positive T cell function, and promotes M2 macrophage polarization and fibroblast activation [30]. The immune microenvironment analysis in this study further validated this mechanism:In the high-risk group, there was a significant increase in the infiltration of M2 macrophages (14.2% vs. 8.6%) and regulatory T cells (6.8% vs. 4.4%), while the infiltration of CD8-positive T cells (18.6% vs. 12.4%) and M1 macrophages (6.8% vs. 4.2%) was significantly reduced. These changes in immune cell

composition were highly consistent with the activation of the TGF-β signaling pathway, collectively contributing to an immunosuppressive tumor microenvironment.Single-sample gene set enrichment analysis similarly confirmed that the TGF-β signaling pathway and hypoxia-related pathways were significantly enriched in the high-risk group, whereas antigen presentation, T-cell activation, and interferon-γ response pathways were enriched in the favorable-prognosis group. These findings suggest that abnormal activation of the TGF-β signaling pathway in elderly lung cancer patients may drive immune evasion by remodeling the tumor microenvironment, thereby leading to immunotherapy failure.The uniqueness of this study lies in its integration of deep learning-based imaging prediction models with bioinformatics mechanism studies to explore the molecular basis underlying imaging phenotypes. Through cross-dataset association analysis, this study found that among the 86 genes significantly associated with high imaging risk scores, 8 overlapped with polygenic prognostic features, including COL11A1,THBS2, MMP11, SPP1, POSTN, FN1, TIMP1, and LOXL2. Functional enrichment analysis revealed that these genes are primarily involved in extracellular matrix remodeling, the TGF-β signaling pathway, and epithelial-mesenchymal transition. This finding suggests that the high imaging risk features identified by the deep learning model may reflect excessive extracellular matrix deposition, fibrotic changes, and an immunosuppressive state within the tumor microenvironment.

Based on these findings, this study proposes the following hypothesis: In elderly lung cancer patients, certain tumors with a highly invasive phenotype exhibit high expression of genes associated with extracellular matrix remodeling, leading to abnormal deposition of collagen fibers and increased matrix stiffness in the tumor microenvironment. These physical changes promote the epithelial-mesenchymal transition and migratory capacity of tumor cells through mechanical signaling pathways, while simultaneously creating an immunosuppressive microenvironment by affecting the infiltration and function of immune cells. Specifically, a dense extracellular matrix physically impedes the infiltration of CD8-positive T cells while simultaneously inducing M2-type macrophage polarization and regulatory T cell expansion by activating the TGF-β signaling pathway, thereby suppressing antitumor immune responses.These biological processes may manifest on CT images as irregular tumor margins, increased internal heterogeneity, and indistinct boundaries with surrounding tissues; deep learning models predict prognosis by automatically learning these imaging features [22–24]. This hypothesis provides a theoretical framework for

understanding the biological basis of radiological predictive results and suggests that interventions targeting extracellular matrix remodeling and the TGF-β signaling pathway may serve as new strategies to improve the efficacy of immunotherapy for lung cancer in the elderly.

This study has the following limitations, which need to be addressed in future research. First, the CT image data used in this study were sourced from the TCIA public database. Although TCIA provides imaging data matched to TCGA patients, there is heterogeneity in imaging equipment and parameters. Despite preprocessing steps such as image resampling and grayscale normalization, differences in images across different devices may still affect model performance. Second, the bioinformatics analysis in the second part of this study was based on public databases, in which the majority of patients did not receive immunotherapy but were included in survival analyses based on natural disease progression. Although this study used the GEO immunotherapy dataset for external validation, the direct association between transcriptomic features and immunotherapy prognosis still needs to be validated in a larger immunotherapy cohort. Third, this study did not conduct a dedicated analysis of patients with hyperprogression. Hyperprogression is a clinically significant phenomenon in immunotherapy; its incidence and predictive factors in elderly patients remain unclear, and this represents an important future research direction in this field. These limitations suggest that the findings of this study require further validation in larger-scale, prospective, multicenter studies.

Conclusion

Based on public databases, this study developed a risk stratification model for the immune microenvironment in elderly lung cancer patients, forming a complete research cycle from imaging assessment to mechanistic interpretation.The deep learning fusion model outperformed traditional clinical models in risk discrimination (C-index: 0.748 vs. 0.668), and the median OS in the high-risk group was significantly shorter than that in the low-risk group. At the molecular level, the high-risk group exhibited a typical immunosuppressive phenotype characterized by increased M2 macrophage infiltration, reduced $CD8^+$ T-cell infiltration, and activation of the TGF-β signaling pathway; GEO immunotherapy data confirmed that progression-free survival was

significantly shorter in high-risk patients following immunotherapy. Imaging-molecular correlation analysis confirmed that the imaging risk features identified by deep learning reflect the molecular essence of extracellular matrix remodeling and the immunosuppressive microenvironment. This study provides a non-invasive, accessible tool for identifying elderly lung cancer patients with an extremely low probability of benefiting from immunotherapy, and offers a theoretical basis for using CT imaging as a means of assessing the tumor immune microenvironment. Future studies are needed to further validate its clinical utility in prospective cohorts.

Conflict of Interest Statement

The authors declare that they have no known competing financial interests or personal relationships that could have appeared to influence the work reported in this paper. No funding sources or commercial entities have influenced the study design, data analysis, interpretation, or manuscript preparation.

Funding Statement

This work was funded by the Shandong Traditional Chinese Medicine Science and Technology Project (M20243902).

Ethics Approval and Data Usage Statement

All data used in this study were obtained from publicly available repositories, including The Cancer Genome Atlas (TCGA), The Cancer Imaging Archive (TCIA), the Gene Expression Omnibus (GEO), and the International Cancer Genome Consortium (ICGC). These databases are publicly accessible and have established data use policies that permit secondary analysis for research purposes. As this study involved only retrospective analysis of de-identified, publicly available data, no additional institutional review board approval or informed consent was required. All analyses were conducted in accordance with the data access policies and terms of use of the respective databases.

Consent for Publication

Not applicable. This study used only publicly available, de-identified data from TCGA, TCIA, GEO, and ICGC; no direct human participant involvement occurred.

Data Availability and Reproducibility Statement

All data used in this study are publicly accessible through the TCGA, TCIA, GEO, and ICGC portals.

Clinical Trial Number

Not applicable.

References

[1] Sung H, Ferlay J, Siegel RL, et al. Global Cancer Statistics 2020: GLOBOCAN Estimates of Incidence and Mortality Worldwide for 36 Cancers in 185 Countries. CA: A Cancer Journal for Clinicians. 2021;71(3):209-249.

[2] Siegel RL, Miller KD, Fuchs HE, et al. Cancer Statistics, 2022. CA: A Cancer Journal for Clinicians. 2022;72(1):7-33.

[3] Li Q, Xia C, Li H, et al. Disparities in 36 cancers across 185 countries: secondary analysis of global cancer statistics. Front Med. 2024;18(5):911-920. [4] Burdett N, Vincent AD, O'Callaghan M, Kichenadasse G. Competing Risks in Older Patients With Cancer: A Systematic Review of Geriatric Oncology Trials. J Natl Cancer Inst. 2018;110(8):825-830. [5] Talarico L, Chen G, Pazdur R. Enrollment of elderly patients in clinical trials for cancer drug registration: a 7-year experience by the US Food and Drug Administration. J Clin Oncol. 2004;22(22):4626-4631. [6] Reck M, Rodríguez-Abreu D, Robinson AG, et al. Pembrolizumab versus Chemotherapy for PD-L1-Positive Non-Small-Cell Lung Cancer. New England Journal of Medicine.

2016;375(19):1823-1833.

[7] Mok TSK, Wu YL, Kudaba I, et al. Pembrolizumab versus chemotherapy for previously untreated, PD-L1-expressing, locally advanced or metastatic non-small-cell lung cancer (KEYNOTE-042): a randomised, open-label, controlled, phase 3 trial. The Lancet. 2019;393(10183):1819-1830.

[8] Gandhi L, Rodríguez-Abreu D, Gadgeel S, et al. Pembrolizumab plus Chemotherapy in Metastatic Non-Small-Cell Lung Cancer. New England Journal of Medicine. 2018;378(22):2078-2092.

[9] Elkrief A, Richard C, Malo J, et al. Efficacy of immune checkpoint inhibitors in older patients with non-small cell lung cancer: Real-world data from multicentric cohorts in Canada and France. J Geriatr Oncol. 2020;11(5):802-806.

[10] Bertaglia V, Petrelli F, Dottorini L, et al. Chemotherapy plus immunotherapy as first line combination in older patients with extensive stage small cell lung cancer: A systematic review and meta-analysis. Semin Oncol. 2025;52(1):14-18. [11] Mailly-Giacchetti L, Lopez-Trabada D, Feldman J, André T, Cohen R. Tolérance et efficacité des inhibiteurs de points de contrôle immunitaire en monothérapie chez les patients âgés [Safety and efficacy of immune checkpoint inhibitors in elderly patients]. Bull Cancer. 2023;110(11):1204-1214. [12] Yang S, Zhu Y, Liu S, Xiao K. A Retrospective Study of First-Line Immunotherapy for Advanced Non-Small Cell Lung Cancer in the Elderly. Aging Med (Milton). 2025;8(6):592-611. Published 2025 Dec 26. [13] Salem JE, Manouchehri A, Moey M, et al. Cardiovascular toxicities associated with immune checkpoint inhibitors: an observational, retrospective, pharmacovigilance study. The Lancet Oncology. 2018;19(12):1579-1589.

[14] Ferrara R, Mezquita L, Texier M, et al. Hyperprogressive Disease in Patients With Advanced Non-Small Cell Lung Cancer Treated With PD-1/PD-L1 Inhibitors or With Single-Agent Chemotherapy. JAMA Oncol. 2018;4(11):1543-1552. [15] Ding Y, Lei S, Wang L, et al. Age-related efficacy of immunotherapies in advanced non-small cell lung cancer: a comprehensive meta-analysis. Lung Cancer. 2024;195:107925.

[16] Chalmers ZR, Connelly CF, Fabrizio D, et al. Analysis of 100,000 human cancer genomes reveals the landscape of tumor mutational burden. Genome Medicine. 2017;9(1):34.

[17]Rakaee M, Tafavvoghi M, Ricciuti B, et al. Deep Learning Model for Predicting

Immunotherapy Response in Advanced Non-Small Cell Lung Cancer. JAMA Oncol. 2025;11(2):109-118.

[18] Mezquita L, Auclin E, Ferrara R, et al. Association of the Lung Immune Prognostic Index with immune checkpoint inhibitor outcomes in patients with advanced non-small cell lung cancer. JAMA Oncology. 2018;4(3):351-357.

[19] LeCun Y, Bengio Y, Hinton G. Deep learning. Nature. 2015;521(7553):436-444.

[20] Isensee F, Jaeger PF, Kohl SAA, et al. nnU-Net: a self-configuring method for deep learning-based biomedical image segmentation. Nature Methods. 2021;18(2):203-211.

[21] Xu Y, Hosny A, Zeleznik R, et al. Deep learning predicts lung cancer treatment response from serial medical imaging. Clinical Cancer Research. 2019;25(11):3266-3275.

[22] Sun R, Limkin EJ, Vakalopoulou M, et al. A radiomics approach to assess tumour-infiltrating CD8 cells and response to anti-PD-1 or anti-PD-L1 immunotherapy: an imaging biomarker, retrospective multicohort study. The Lancet Oncology. 2018;19(9):1180-1191.

[23] Wu Y, Zhang W, Liang X, et al. Habitat radiomics analysis for progression free survival and immune-related adverse reaction prediction in non-small cell lung cancer treated by immunotherapy. J Transl Med. 2025;23(1):393. Published 2025 Apr 3.

[24] Liu X, Li KW, Yang R, Geng LS. Review of Deep Learning Based Automatic Segmentation for Lung Cancer Radiotherapy. Front Oncol. 2021;11:717039. Published 2021 Jul 8. [25] Vithayathil M, Koku D, Campani C, et al. Machine learning based radiomic models outperform clinical biomarkers in predicting outcomes after immunotherapy for hepatocellular carcinoma. J Hepatol. 2025;83(4):959-970.

[26] Cancer Genome Atlas Research Network. Comprehensive genomic characterization of squamous cell lung cancers. Nature. 2012;489(7417):519-525.

[27] Newman AM, Liu CL, Green MR, et al. Robust enumeration of cell subsets from tissue expression profiles. Nature Methods. 2015;12(5):453-457.

[28] Yoshihara K, Shahmoradgoli M, Martínez E, et al. Inferring tumour purity and stromal and immune cell admixture from expression data. Nature Communications. 2013;4:2612.

[29] Langfelder P, Horvath S. WGCNA: an R package for weighted correlation network analysis. BMC Bioinformatics. 2008;9:559.

[30] Lian J, Yue Y, Yu W, et al. Immunosenescence: a key player in cancer development. Journal

of Hematology and Oncology. 2020;13(1):151.

[31] Ma B, Ran R, Liao HY, Zhang HH. The paradoxical role of matrix metalloproteinase-11 in cancer. Biomed Pharmacother. 2021;141:111899.

[32] Shirakawa K, Sano M, Sakane I, et al. Interleukin-7 receptor activation in interstitial macrophages promotes lung fibrosis through secreted phosphoprotein 1. Am J Respir Cell Mol Biol. 2026;74(5):644-660.

Figures

Figure 1. Flowchart of the overall study design.

Figure 2 Architecture and performance evaluation of the deep learning model for medical imaging.

(A) 3D ResNet architecture diagram showing the complete process from 3D CT input to a 512-dimensional feature vector, including four residual modules (channel counts: 64 → 128 → 256 → 512) and a global average pooling layer. (B) Representative example of automatic tumor segmentation using nnU-Net. (C) Violin plot of the Dice coefficient distribution, stratified by tumor size (≤3 cm vs. >3 cm) and location (central vs. peripheral). (D) Three-stage Sankey diagram of feature selection: 512 → 186 → 98 → 26 features. (E) Bar chart comparing model performance, showing the C-index of the clinical Cox model, the imaging Cox model, and the DeepSurv fusion model, with error bars and P-values. (F) Time-dependent ROC curves showing the AUC of the DeepSurv model for predicting 6-, 12-, and 24-month overall survival. (G) SHAP model interpretability analysis.

Figure 3 Analysis of differentially expressed genes and functional enrichment.

(A) Volcano plot of differentially expressed genes. (B) Clustering heatmap of the top 50 differentially expressed genes. (C) GO biological process enrichment bubble plot of upregulated genes, showing the top 15 significantly enriched biological processes. (D) KEGG pathway enrichment bar chart, showing the top 10 significantly enriched pathways for upregulated and downregulated genes.

Figure 4 Analysis of tumor immune microenvironment characteristics and weighted gene co-expression networks.

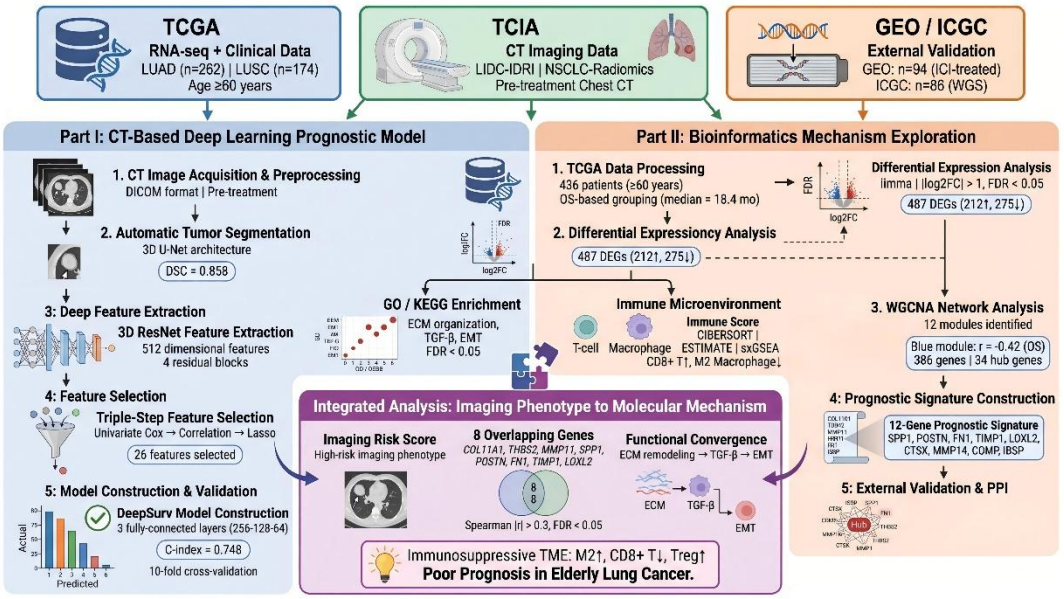
(A) CIBERSORT immune cell infiltration stacked bar chart. (B) ESTIMATE score box plot. (C) ssGSEA heatmap of immune-related pathway enrichment, showing differences in enrichment scores between the two groups for pathways such as antigen presentation, T-cell activation, interferon-γ response, TGF-β signaling, and hypoxia.

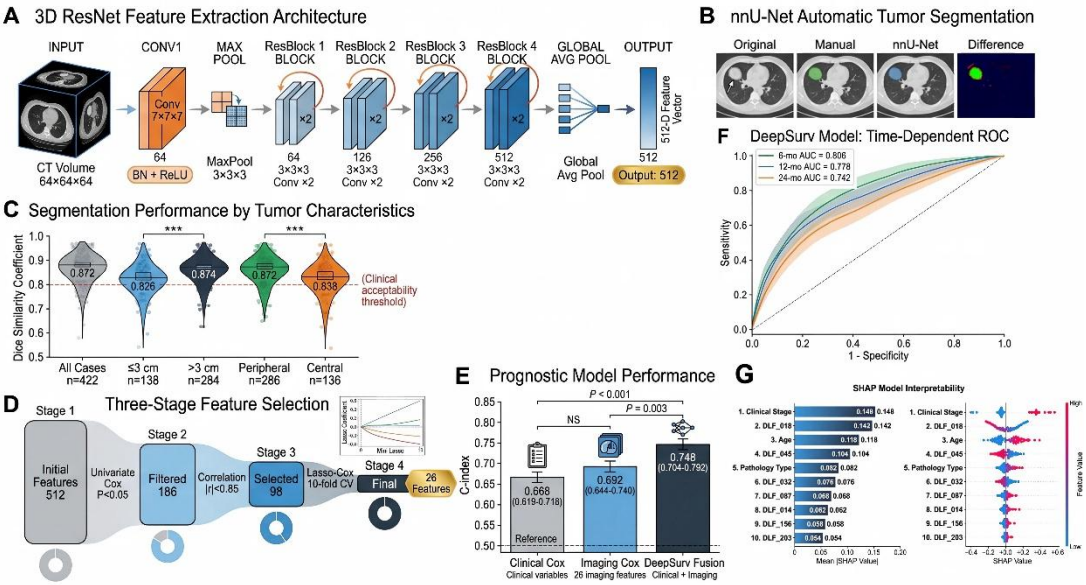
Figure 5 Construction and validation of multigene prognostic features.

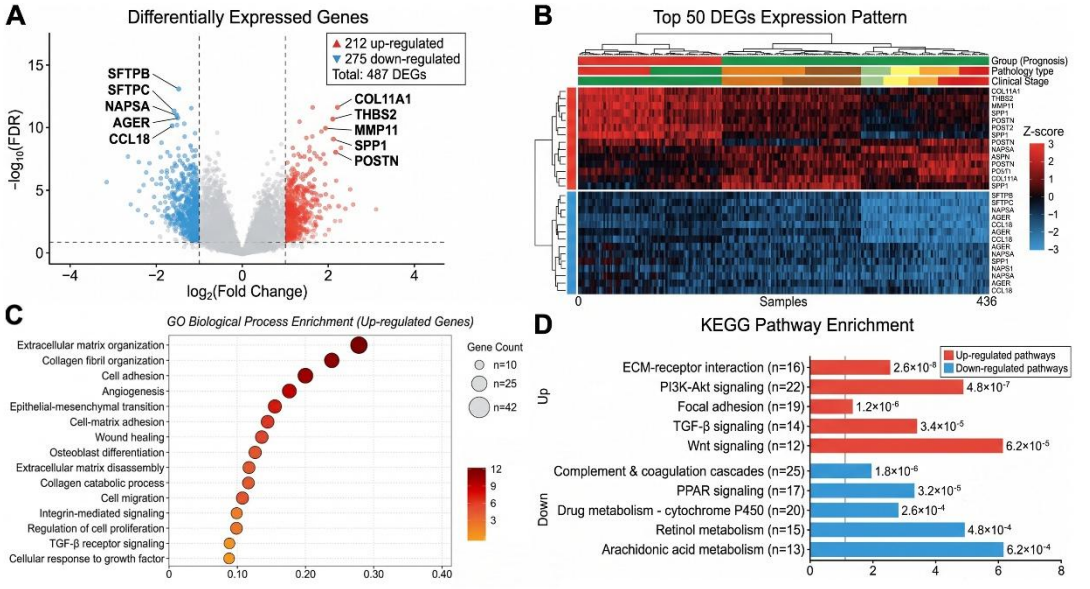
(A) Lasso regression error curves for 10-fold cross-validation. (B) Lasso regression coefficient path map. (C) Kaplan-Meier survival curves for the TCGA training set. (D) Kaplan-Meier survival curves for the ICGC external validation set. (E) Time-dependent ROC curves.

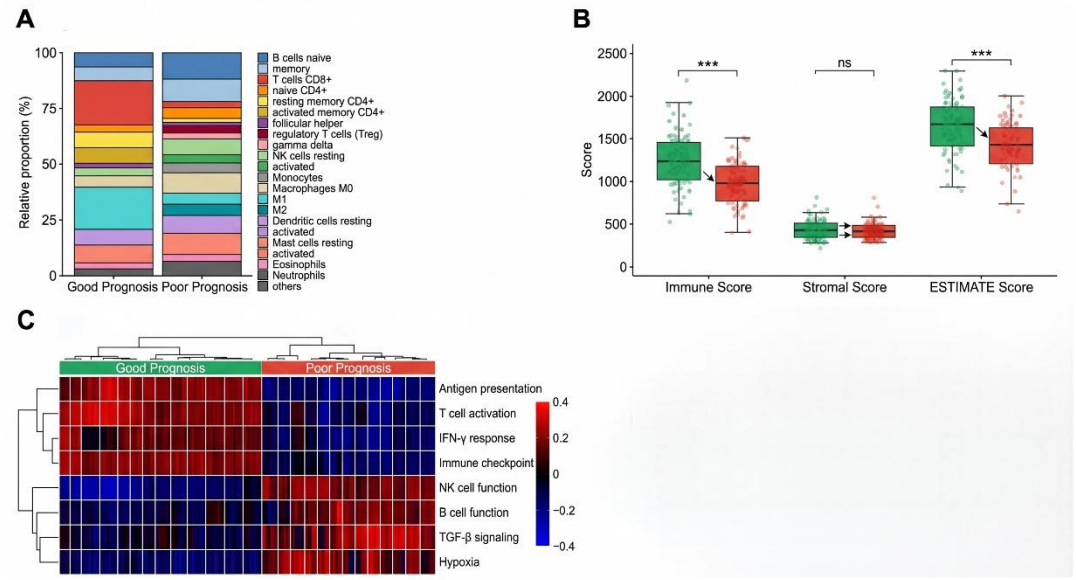
Figure 6 Protein-protein interaction network, core hub genes, and the imaging-molecular integration hypothesis model.

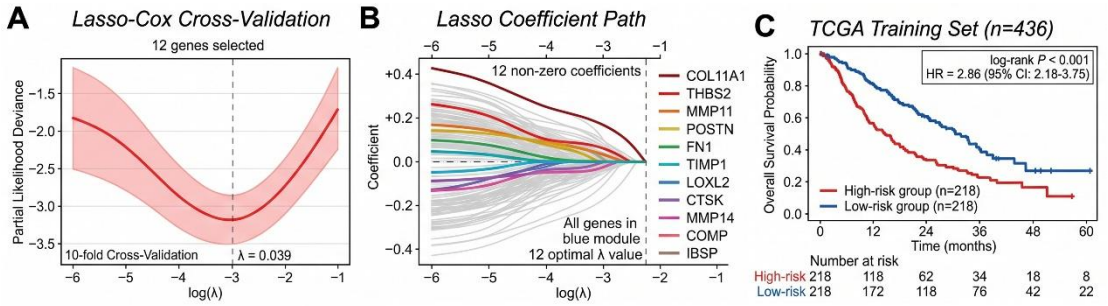
(A) Protein-protein interaction network of 12 prognostic genes. (B) Combined single-gene Kaplan-Meier survival curves for 5 core hub genes. (C) Box plots showing expression differences of the 5 core hub genes in Stage III and Stage IV patients. (D) Schematic diagram of the imaging-molecular integration hypothesis.

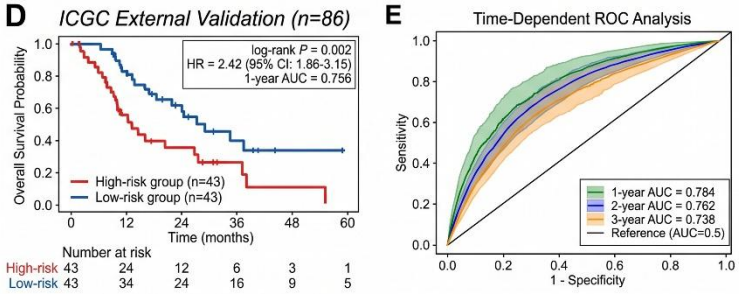

TCGA
RNA-seq + Clinical Data
LUAD (n=262) | LUSC (n=174)
Age ≥60 years
TCIA
CT Imaging Data
LIDC-IDRI | NSCLC-Radiomics
Pre-treatment Chest CT
GEO / ICGC
External Validation
GEO: n=94 (ICI-treated)
ICGC: n=86 (WGS)
Part I: CT-Based Deep Learning Prognostic Model
1. CT Image Acquisition & Preprocessing
DICOM format | Pre-treatment
2. Automatic Tumor Segmentation
3D U-Net architecture
DSC = 0.858
3: Deep Feature Extraction
3D ResNet Feature Extraction
512 dimensional features
4 residual blocks
4: Feature Selection
Triple-Step Feature Selection
Univariate Cox → Correlation → Lasso
26 features selected
5: Model Construction & Validation
DeepSurv Model Construction
3 fully-connected layers (256-128-64)
C-index = 0.748
10-fold cross-validation
Part II: Bioinformatics Mechanism Exploration
1. TCGA Data Processing
436 patients (≥60 years)
OS-based grouping (median = 18.4 mo)
Differential Expression Analysis
limma | |log2FC| > 1, FDR < 0.05
487 DEGs (212↑, 275↓)
2. Differential Expressiony Analysis
487 DEGs (212↑, 275↓)
GO / KEGG Enrichment
ECM organization,
TGF-β, EMT
FDR < 0.05
Immune Microenvironment
Immune Score
CIBERSORT | ESTIMATE | ssGSEA
T-cell
Macrophage
CD8+ T↑, M2 Macrophage↓
3. WGCNA Network Analysis
12 modules identified
Blue module: r = -0.42 (OS)
386 genes | 34 hub genes
4: Prognostic Signature Construction
12-Gene Prognostic Signature
SPP1, POSTN, FN1, TIMP1, LOXL2,
CTSK, MMP14, COMP, IBSP
5: External Validation & PPI
Integrated Analysis: Imaging Phenotype to Molecular Mechanism
Imaging Risk Score
High-risk imaging phenotype
8 Overlapping Genes
COL11A1, THBS2, MMP11, SPP1,
POSTN, FN1, TIMP1, LOXL2
Spearman |r| > 0.3, FDR < 0.05
Functional Convergence
ECM remodeling → TGF-β → EMT
ECM
TGF-β
EMT
Immunosuppressive TME: M2↑, CD8+ T↓, Treg↑
Poor Prognosis in Elderly Lung Cancer.

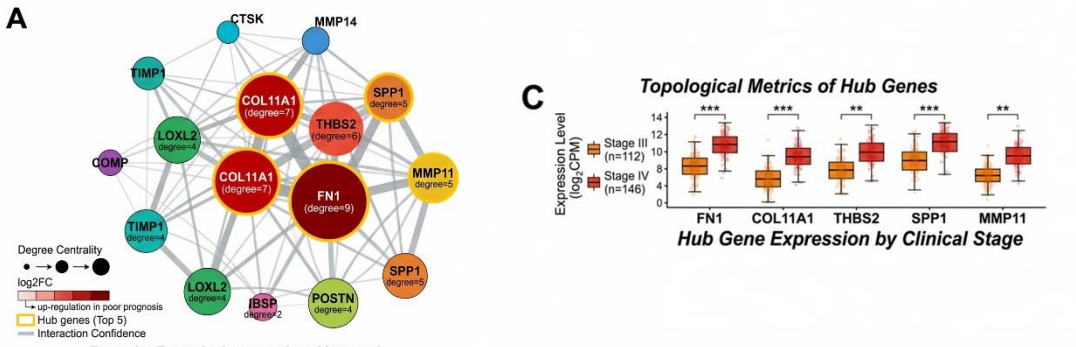

A 3D ResNet Feature Extraction Architecture
INPUT
CONV1
MAX POOL
ResBlock 1 BLOCK
ResBlock 2 BLOCK
ResBlock 3 BLOCK
ResBlock 4 BLOCK
GLOBAL AVG POOL
OUTPUT
CT Volume 64×64×64
Conv 7×7×7
64
BN + ReLU
MaxPool 3×3×3
64 3×3×3 Conv ×2
126 3×3×3 Conv ×2
256 3×3×3 Conv ×2
512 3×3×3 Conv ×2
Global Avg Pool
512
Output: 512
512-D Feature Vector
B nnU-Net Automatic Tumor Segmentation
Original
Manual
nnU-Net
Difference
C Segmentation Performance by Tumor Characteristics
Dice Similarity Coefficient
0.872
0.826
0.874
0.872
0.838
(Clinical acceptability threshold)
All Cases n=422
≤3 cm n=138
>3 cm n=284
Peripheral n=286
Central n=136
D Three-Stage Feature Selection
Stage 1
Initial Features 512
Univariate Cox P<0.05
Stage 2
Filtered 186
Correlation |r|<0.85
Stage 3
Selected 98
Lasso-Cox 10-fold CV
Stage 4
Final
26 Features
E Prognostic Model Performance
P < 0.001
P = 0.003
NS
C-index
0.668 (0.619-0.718)
Reference
0.692 (0.644-0.740)
0.748 (0.704-0.792)
Clinical Cox
Clinical variables
Imaging Cox
26 imaging features
DeepSurv Fusion
Clinical + Imaging
F DeepSurv Model: Time-Dependent ROC
6-mo AUC = 0.806
12-mo AUC = 0.778
24-mo AUC = 0.742
Sensitivity
1 - Specificity
G
SHAP Model Interpretability
1. Clinical Stage
2. DLF_018
3. Age
4. DLF_045
5. Pathology Type
6. DLF_032
7. DLF_087
8. DLF_014
9. DLF_156
10. DLF_293
Mean |SHAP Value|
SHAP Value
Feature Value

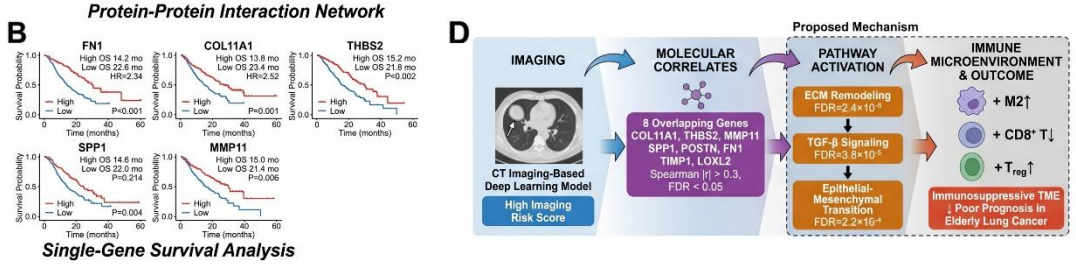

A Differentially Expressed Genes
212 up-regulated
275 down-regulated
Total: 487 DEGs
SFTPB
SFTPC
NAPSA
AGER
CCL18
COL11A1
THBS2
MMP11
SPP1
POSTN
−log10(FDR)
log2(Fold Change)
B Top 50 DEGs Expression Pattern
Group (Prognosis)
Pathology type
Clinical Stage
Z-score
Samples
C GO Biological Process Enrichment (Up-regulated Genes)
Extracellular matrix organization
Collagen fibril organization
Cell adhesion
Angiogenesis
Epithelial-mesenchymal transition
Cell-matrix adhesion
Wound healing
Osteoblast differentiation
Extracellular matrix disassembly
Collagen catabolic process
Cell migration
Integrin-mediated signaling
Regulation of cell proliferation
TGF-β receptor signaling
Cellular response to growth factor
Gene Count
n=10
n=25
n=42
D KEGG Pathway Enrichment
Up-regulated pathways
Down-regulated pathways
Up
Down
ECM-receptor interaction (n=16) 2.6×10⁻⁶
PI3K-Akt signaling (n=22) 4.8×10⁻⁷
Focal adhesion (n=19) 1.2×10⁻⁶
TGF-β signaling (n=14) 3.4×10⁻⁵
Wnt signaling (n=12) 6.2×10⁻⁵
Complement & coagulation cascades (n=25) 1.8×10⁻⁶
PPAR signaling (n=17) 3.2×10⁻⁵
Drug metabolism - cytochrome P450 (n=20) 2.6×10⁻⁴
Retinol metabolism (n=15) 4.8×10⁻⁴
Arachidonic acid metabolism (n=13) 6.2×10⁻⁴


A
Relative proportion (%)
Good Prognosis
Poor Prognosis
B cells naive
memory
T cells CD8+
naive CD4+
resting memory CD4+
activated memory CD4+
follicular helper
regulatory T cells (Treg)
gamma delta
NK cells resting
activated
Monocytes
Macrophages M0
M1
M2
Dendritic cells resting
activated
Mast cells resting
activated
Eosinophils
Neutrophils
others
B
Score
Immune Score
Stromal Score
ESTIMATE Score
***
ns
***
C
Good Prognosis
Poor Prognosis
Antigen presentation
T cell activation
IFN-γ response
Immune checkpoint
NK cell function
B cell function
TGF-β signaling
Hypoxia


A
Lasso-Cox Cross-Validation
12 genes selected
Partial Likelihood Deviance
10-fold Cross-Validation
λ = 0.039
log(λ)
B
Lasso Coefficient Path
12 non-zero coefficients
Coefficient
All genes in blue module
12 optimal λ value
log(λ)
COL11A1
THBS2
MMP11
POSTN
FN1
TIMP1
LOXL2
CTSK
MMP14
COMP
IBSP
C
TCGA Training Set (n=436)
log-rank P < 0.001
HR = 2.86 (95% CI: 2.18-3.75)
Overall Survival Probability
High-risk group (n=218)
Low-risk group (n=218)
Time (months)
Number at risk
High-risk 218 118 62 34 18 8
Low-risk 218 172 118 76 42 22


D
ICGC External Validation (n=86)
log-rank P = 0.002
HR = 2.42 (95% CI: 1.86-3.15)
1-year AUC = 0.756
Overall Survival Probability
High-risk group (n=43)
Low-risk group (n=43)
Time (months)
Number at risk
High-risk 43 24 12 6 3 1
Low-risk 43 34 24 16 9 5
E
Time-Dependent ROC Analysis
Sensitivity
1 - Specificity
1-year AUC = 0.784
2-year AUC = 0.762
3-year AUC = 0.738
Reference (AUC=0.5)


A
CTSK
MMP14
TIMP1
COL11A1 (degree=7)
SPP1 degree=5
THBS2 (degree=6)
LOXL2 degree=4
COMP
COL11A1 (degree=7)
FN1 (degree=9)
MMP11 degree=5
TIMP1 degree=4
SPP1 degree=5
LOXL2 degree=4
IBSP degree=2
POSTN degree=4
Degree Centrality
log2FC
up-regulation in poor prognosis
Hub genes (Top 5)
Interaction Confidence
Protein-Protein Interaction Network
C
Topological Metrics of Hub Genes
Expression Level (log2CPM)
Stage III (n=112)
Stage IV (n=146)
FN1
COL11A1
THBS2
SPP1
MMP11
Hub Gene Expression by Clinical Stage


B
FN1
High OS 14.2 mo
Low OS 22.6 mo
HR=2.34
P<0.001
COL11A1
High OS 13.8 mo
Low OS 23.4 mo
HR=2.52
P<0.001
THBS2
High OS 15.2 mo
Low OS 21.8 mo
P<0.002
SPP1
High OS 14.6 mo
Low OS 22.0 mo
P=0.214
P=0.004
MMP11
High OS 15.0 mo
Low OS 21.4 mo
P=0.006
Survival Probability
Time (months)
High
Low
Single-Gene Survival Analysis
D
Proposed Mechanism
IMAGING
CT Imaging-Based Deep Learning Model
High Imaging Risk Score
MOLECULAR CORRELATES
8 Overlapping Genes
COL11A1, THBS2, MMP11
SPP1, POSTN, FN1
TIMP1, LOXL2
Spearman |r| > 0.3, FDR < 0.05
PATHWAY ACTIVATION
ECM Remodeling
FDR=2.4×10⁻⁵
TGF-β Signaling
FDR=3.8×10⁻⁵
Epithelial-Mesenchymal Transition
FDR=2.2×10⁻⁴
IMMUNE MICROENVIRONMENT & OUTCOME
+ M2↑
+ CD8⁺ T↓
+ Treg↑
Immunosuppressive TME
↓ Poor Prognosis in Elderly Lung Cancer

Supplementary Files

This is a list of supplementary files associated with this preprint. Click to download.

- Table1.docx
- Table3.docx
- Table2.docx
- Table4.docx